Angular Memory Effect of Transmission Eigenchannels

Hasan Yılmaz,[1] Chia Wei Hsu,[1,2] Arthur Goetschy,[3] Stefan Bittner,[1] Stefan Rotter,[4] Alexey Yamilov,[5] and Hui Cao[1,*]

[1]Department of Applied Physics, Yale University, New Haven, Connecticut 06520, USA
[2]Ming Hsieh Department of Electrical and Computer Engineering, University of Southern California, Los Angeles, California 90089, USA
[3]ESPCI Paris, PSL University, CNRS, Institut Langevin, 1 rue Jussieu, F-75005 Paris, France
[4]Institute for Theoretical Physics, Vienna University of Technology (TU Wien), 1040 Vienna, Austria
[5]Department of Physics, Missouri University of Science & Technology, Rolla, Missouri 65409, USA

(Received 14 June 2019; published 12 November 2019)

The optical memory effect has emerged as a powerful tool for imaging through multiple-scattering media; however, the finite angular range of the memory effect limits the field of view. Here, we demonstrate experimentally that selective coupling of incident light into a high-transmission channel increases the angular memory-effect range. This enhancement is attributed to the robustness of the high-transmission channels against perturbations such as sample tilt or wave front tilt. Our work shows that the high-transmission channels provide an enhanced field of view for memory-effect-based imaging through diffusive media.

DOI: 10.1103/PhysRevLett.123.203901

"Seeing through an opaque medium" has long been a grand challenge, as ballistic light decays exponentially with depth. Various techniques have been developed to extract the weak signal from single or few scattering in an overwhelming background of multiply scattered light [1–5]. A recent paradigm shift is harnessing multiply scattered or diffused light for imaging applications [6–11]. The key ingredient that enabled this strategic shift is the hidden correlations of seemingly random speckles formed by the interference of scattered light [12–16]. Quite remarkably, such correlations have been both predicted and observed in the angular, spectral, spatial, and temporal domains [17–30].

Perhaps the best known from all of the above correlations is the angular "memory effect": when the incident wave front of a coherent beam on a diffusive medium is tilted by a small angle, the transmitted wave front is tilted by the same amount, resulting in the translation of the far-field speckle pattern [25–29] [see Fig. 1(a)]. The angular memory effect originates from the intrinsic correlations in the transmission matrix t of a diffusive slab with a width W that is much larger than its length L [27,29,30]. In real space, t is a banded matrix, because a point excitation at the front surface emerges as a diffuse halo of radius L at the back surface of the slab. In the spatial-frequency domain, t displays correlations between the matrix elements along the diagonal. The diagonal correlations are the origin of the memory effect with an angular correlation width $\theta_0 = \lambda/(2\pi L)$, where λ is the wavelength of light. While the memory effect has already enabled various applications in imaging [12–16], its limited angular correlation width remains a central obstacle for wide-field imaging.

A recent breakthrough in coherent control of light in diffusive media is the selective excitation of transmission eigenchannels by wave front shaping [31–35]. It allows us not only to vary the transmittance from near zero to the order of unity, but also to drastically change the spatial distribution of energy density inside the medium [35–40]. Moreover, it has very recently been discovered that in a wide diffusive slab, the transmission eigenchannels are localized in the transverse directions and have the same transverse width at the front and the back surfaces of the slab (i.e., there is no transverse spreading) [41,42]. Since the transverse spreading of scattered waves is inherently connected to the theory behind the angular memory effect, the absence of spreading immediately raises the question whether and how the angular memory effect is modified for transmission eigenchannels and whether one could make use of such modifications to increase the angular memory-effect range.

In this Letter, we investigate this question experimentally and numerically by studying the angular memory effect of transmission eigenchannels in wide diffusive slabs. Compared to random incident wave fronts, we find that the angular memory-effect range is enhanced for high-transmission channels, but reduced for low-transmission channels. These phenomena can be explained by the robustness of the transmission eigenchannels against sample tilt or incident wave front tilt. Our work illustrates the significance of high-transmission channels in memory-effect-based imaging applications: they not only penetrate deeper inside a diffusive medium, but also provide a wider field of view due to their enhanced angular memory-effect range. Furthermore, we observe the opposite behavior in

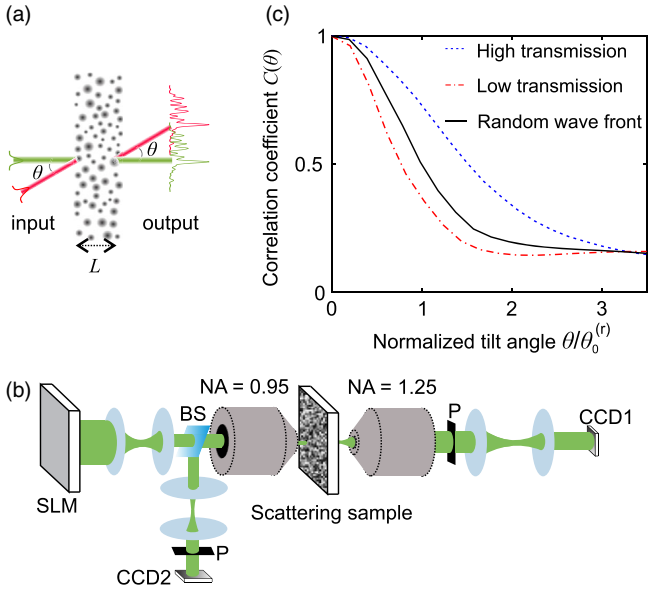

FIG. 1. Angular memory effect, the experimental setup, and data. (a) Sketch of the angular memory effect for a diffusive slab. An incident beam generates a transmitted speckle pattern in far field (green). When the input wave front is tilted by a small angle θ, the output wave front is tilted by the same angle θ, leading to a lateral shift of far-field speckle pattern (red). (b) Simplified schematic of the experimental setup. The laser beam is modulated by a phase-only SLM, imaged onto the pupil of a microscope objective by a pair of lenses, and directed onto a ZnO nanoparticle film. The transmitted (reflected) light is measured by a CCD camera CCD1 (CCD2) in the far field. NA and P stand for numerical aperture and linear polarizer, respectively. (c) Experimentally measured intensity correlation function $C(\theta)$ of the transmitted speckle patterns as a function of the normalized tilt angle $\theta/\theta_0^{(r)}$, for a high-transmission channel (with $T/\bar{T} = 2.29$, blue dashed line), a low-transmission channel (with $T/\bar{T} = 0.58$, red dot-dashed line), and a random incident wave front (black solid line). $\theta_0^{(r)}$ denotes the width of $C(\theta)$ for the random wave fronts where $C(\theta_0^{(r)}) = C(0)/2$, and its value is about 1°.

reflection, where the angular memory-effect range is reduced for high-transmission channels but enhanced for low-transmission channels. This result suggests that the angular memory-effect range of reflected light may be used as a signature of coupling light into high-transmission channels in experiments where there is no access to the light field behind scattering media [43–45].

Experimentally, we measure the angular memory effect by selectively coupling coherent light into a single transmission eigenchannel. The scattering sample consists of densely packed zinc oxide (ZnO) nanoparticles spin coated on a cover slip. The thickness of the ZnO layer $L \simeq 10$ μm is much smaller than its transverse dimensions (2 cm × 2 cm). Since the transport mean free path $l_t \simeq 1.5$ μm is much shorter than L, light transport in the sample is diffusive. The measured transmittance averaged over random incident wave fronts is $\bar{T} \simeq 0.2$.

To find the transmission eigenchannels, we measure the field transmission matrix t with the setup shown in Fig. 1(b) [46]. A monochromatic laser beam of wavelength $\lambda = 532$ nm is modulated by a phase-only spatial light modulator (SLM) before impinging on the sample. The transmitted field is measured by common-path interferometry with a CCD camera [41,47,51]. We modulate two orthogonal polarizations of the incident field and record one linear polarization of the transmitted light. The field transmission matrix is obtained in spatial-frequency space. The incident wave front V_n of a transmission eigenchannel is determined from $t^\dagger t V_n = \tau_n V_n$, where τ_n is the nth transmission eigenvalue (ordered from high to low τ_n). We display the phase front of V_n on the SLM, and record the far-field intensity pattern of the transmitted field $I(0)$ with the CCD camera. We then tilt an eigenchannel wave front incident onto the sample by angle θ and track the change in the transmitted wave front. The transmitted intensity pattern $I(\theta)$ on the camera is numerically tilted back by θ, and its Pearson correlation with the original pattern $I(0)$ is computed as $C(\theta) = \langle \delta I(0) \delta I(\theta) \rangle / (\langle \delta I(0)^2 \rangle^{1/2} \langle \delta I(\theta)^2 \rangle^{1/2})$, where $\delta I \equiv I - \langle I \rangle$ and $\langle \cdots \rangle$ represents spatial averaging over the output pattern. We calculate the intensity correlation coefficient $C(\theta)$ of the ten highest transmission channels, of the ten lowest transmission channels, and of twenty random incident wave fronts. In Fig. 1(c) we show examples of $C(\theta)$ for a high- and a low-transmission channel compared to that of a random wave front: the high-transmission channel decorrelates slower with tilt angle θ than the random wave front, while the low-transmission channel decorrelates faster. $C(\theta)$ does not decay to 0 at large θ due to the limited modulation efficiency of our SLM: as we tilt the incident wave front with the SLM, a small portion of the field remains unmodulated; therefore the corresponding transmitted fields are correlated. From the width of $C(\theta)$, we determine that the angular memory-effect range for the highest transmission channel $\theta_0^{(h)}$ is 1.52 times of that for a random wave front $\theta_0^{(r)}$, and the angular range for the lowest transmission channel is $\theta_0^{(l)} = 0.77\theta_0^{(r)}$.

To confirm that the angular memory effect is enhanced for high-transmission channels and suppressed for low-transmission channels, we numerically simulate light propagation through two-dimensional (2D) diffusive slabs ($W \gg L \gg l_t$). We calculate the complete field transmission matrix t using the recursive Green's function method [46]. Evaluating the transmission eigenchannels of t, we calculate the output fields of each eigenchannel with respect to the tilt angle θ of its incident wave front. The transmitted field is then tilted back by the same angle θ, and its Pearson correlation with the original transmitted field is computed. From the field correlation $C_n^{(E)}(\theta)$, the intensity correlation $C_n(\theta) = |C_n^{(E)}(\theta)|^2$ is obtained. $C_n(\theta)$ decays with the tilt angle θ, and its width $\theta_0^{(n)}$ gives the angular

memory-effect range for the nth eigenchannel. Figure 2(a) clearly shows that $\theta_0^{(n)}$ increases with the transmission eigenvalue τ_n. The eigenchannels with transmittance τ_n above the average value $\bar{\tau}$ have a larger memory-effect range, while those of $\tau_n < \bar{\tau}$ have a smaller memory-effect range than the random wave fronts. Furthermore, we find that the width $\theta_0^{(h)}$ for high-transmission channels is inversely proportional to the effective sample thickness L_{eff} that includes the extrapolation lengths [46].

The numerically observed dependence of the eigenchannel angular memory effect on transmittance agrees qualitatively with the experimental observation. Such a dependence might be surprising at first sight as none of the eigenchannels of the *complete* transmission matrix spreads laterally in the slab, and they all have the same transverse widths at the front and the back sides of the slab [41]. However, we should recognize that once the incident wave front of an eigenchannel is tilted, it is no longer the eigenvector of $t^\dagger t$. Consequently, lateral spreading occurs inside the slab, and the transmitted beam becomes wider than the incident beam for all eigenchannels. The effective widths of input and output beams are given by the participation numbers of the field intensity profiles at the front and the back surfaces of the slab [41]. Their difference ΔD is the transverse spread. As shown in Fig. 2(b), ΔD increases as the tilt angle θ increases. However, the increase is much slower for high-transmission eigenchannels, indicating they are more robust against the tilt of the incident wave front than the low-transmission eigenchannels. This leads to a larger memory-effect range for high-transmission channels than low-transmission ones.

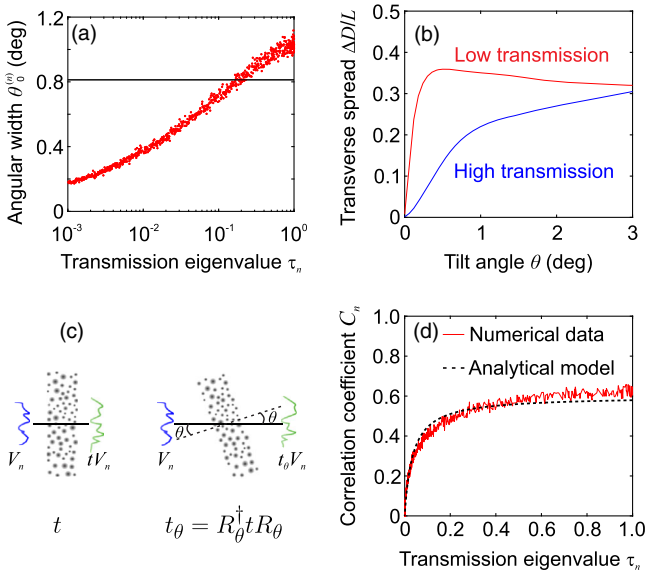

FIG. 2. Numerical and theoretical results. (a) Angular correlation width $\theta_0^{(n)}$ of transmission eigenchannels vs their transmittance τ_n. Each point represents an average over 10 disorder realizations. The horizontal black line denotes the angular correlation width for random incident wave fronts $\theta_0^{(r)}$. (b) Transverse spread ΔD of high ($\bar{\tau} < \tau_n < 1$, blue line) and low ($10^{-4} < \tau_n < \bar{\tau}$, red line) transmission eigenchannels vs tilt angle θ of their incident wave fronts. (c) Sketch of the transmission matrix of a tilted sample $t_\theta = R_\theta^\dagger t R_\theta$, where R_θ is the tilting matrix and t the field transmission matrix without tilting. (d) Intensity correlation coefficient C_n of transmission eigenchannels at the tilt angle $\theta = \theta_0^{(r)} \approx 0.8°$, obtained from numerical simulation (red solid line), and the prediction of the phenomenological model, Eq. (1), with σ^2 as the only fitting parameter (black dashed line). The number of channels is $N = 3239$. The diffusive slabs have thickness $k_0 L = 100$, width $k_0 W = 6000$, transport mean free path $k l_t = 4.6$, average refractive index $n_0 = 1.5$, where $k = n_0 k_0$, $k_0 = 2\pi/\lambda$, and λ is the vacuum wavelength.

The transmission eigenvalue dependence of the tilt-induced lateral spreading shown in Fig. 2(b) can be understood as follows. When the incident wave front of a transmission eigenchannel is tilted by an angle θ, it excites not only this eigenchannel, but also other eigenchannels. The latter can be approximated as a random superposition of all other eigenchannels, which is equivalent to a random incident wave front. The transmitted field profile at the back side of the sample is then a superposition of a transversely localized eigenchannel profile and a transversely spread random wave front profile. For a high-transmission eigenchannel, its output profile dominates over the random wave front profile, but for a low-transmission channel, the output is dominated by the random wave front profile. As a result, the high-transmission channels have stronger correlation and larger memory effect than the low-transmission channels.

To make the above understanding more quantitative, we introduce a phenomenological model that predicts C_n. As illustrated in Fig. 2(c), the angular memory effect can be equivalently considered as the correlation of transmitted fields with respect to the tilt angle θ of the scattering sample for a fixed incident field. The transmission matrix of the tilted sample is $t_\theta = R_\theta^\dagger t R_\theta$, where the tilting matrix is written in the form $R_\theta = \mathbb{1} + X$. We model the matrix X as an $N \times N$ complex random matrix with independent and Gaussian-distributed entries. The variance σ^2/N of its elements determines the amount of perturbation. When the incident wave front corresponds to the transmission eigenchannel V_n of the untilted sample, the transmitted field through the tilted sample is $t_\theta V_n$, and its correlation with the original transmitted field tV_n is

$$C_n \equiv \frac{|\langle V_n|t^\dagger t_\theta|V_n\rangle|^2}{\langle V_n|t^\dagger t|V_n\rangle\langle V_n|t_\theta^\dagger t_\theta|V_n\rangle} \simeq \frac{1}{1+\sigma^2}\frac{\tau_n + \sigma^4\bar{\tau}/N}{\tau_n + \sigma^2\bar{\tau}} \tag{1}$$

(see [46] for the derivation). The prediction of the model fits well to the numerical result [see Fig. 2(d)], with a value

of σ that depends only on θ and the effective sample thickness L_{eff}. In the limit $\theta \ll 1$ rad, it can be shown that $\sigma \propto k_0 L_{\text{eff}} \theta$ [46]. Equation (1) shows that the perturbed output is more correlated with the original output for high-transmission channels, and when $\tau_n \gg \sigma^2 \bar{\tau}$, C_n is on the order of unity. At the same time, the transmitted pattern decorrelates more for low-transmission channels. For $\tau_n \to 0$, C_n is on the order of $1/N$, which is the expected value between two uncorrelated speckle patterns with N speckle grains.

For a fair comparison of the simulation and the experimental data, we must take into account that only a limited number of channels is controlled in the experiment [46]. The limited numerical aperture (NA) in the illumination and the detection, the finite area of illumination on the sample, the phase-only modulation of the (far-field) incident wave fronts, and single-polarization detection of the transmitted light all reduce the range of transmittance of experimentally realized eigenchannels [34,47,52]. Such incomplete control also limits the enhancement or suppression of the angular memory-effect range that can be observed experimentally. Figure 3(a) shows the numerically calculated and the experimentally measured intensity correlation coefficient C_n of transmission eigenchannels vs their normalized transmittance $T/\bar{T}$. The incomplete control reduces the ranges of both C_n and $T/\bar{T}$. Despite the reduced range, the modification of the angular memory effect is clearly observed experimentally and agrees with the simulation result.

A compelling question is raised by the enhanced memory-effect range for high-transmission channels: will the angular memory-effect range also be modified in reflection once light is coupled into a high-transmission channel? To answer this question, we experimentally measure the reflection correlations for individual transmission eigenchannels. The intensity pattern of reflected light is recorded in the far field by a second CCD camera (CCD2) in Fig. 1(b). The modification of the angular correlations in reflection is opposite to the modification in transmission: the high-transmission channels' correlation is smaller in reflection than the low-transmission channels' correlation for a fixed tilt angle $\theta_0^{(r)}$ [see Fig. 3(b)]. The angular correlation width θ_0 in reflection for the highest (lowest) transmission eigenchannel is 7% smaller (6% larger) than that for the random incident wave fronts. Our numerical simulation confirms the experimental observation: the intensity correlation coefficient in reflection $C_n^{(R)}$ decreases as the transmittance increases [Fig. 3(b)]. Taking into account the incomplete control in our experiment, the numerical results are in good agreement with the experimental data.

The modification of the angular memory effect in reflection can also be explained in the framework of our phenomenological model by replacing τ_n by $1 - \tau_n$ [46]. Once the incident light is coupled into a high (low) transmission channel, the reflectance is low (high) and the reflected field pattern is sensitive (robust) to the sample tilt. The reduced memory-effect range in reflection may provide experimental guidance for shaping the incident wave front to couple light into high-transmission channels when there is no access to the transmitted light [43–45].

In summary, we demonstrate that the angular memory effect for individual transmission eigenchannels is distinct from that of random wave fronts. With increasing transmittance, the eigenchannel memory-effect range increases in transmission, but decreases in reflection. Such variations can be explained by our phenomenological model in terms of the robustness of the eigenchannels against perturbations

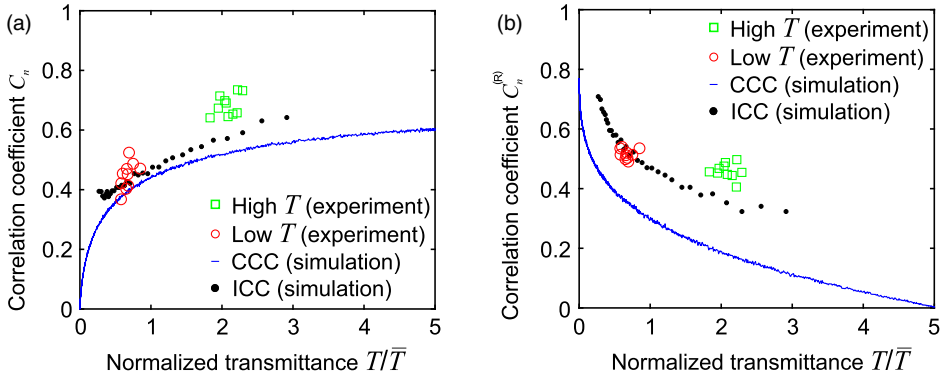

FIG. 3. Comparison between the experimental and the theoretical results. Correlation coefficient C_n in (a) [$C_n^{(R)}$ in (b)] of transmitted (reflected) eigenchannel intensity patterns for $\theta = 0$ and $\theta = \theta_0^{(r)}$ as a function of their normalized transmittance $T/\bar{T}$. $\theta_0^{(r)}$ is the width at half maximum of the angular correlation function in transmission $C(\theta)$ for (a) and in reflection $C^{(R)}(\theta)$ for (b) for random incident wave fronts. Blue solid line and black dots: numerical simulation results in the case of complete channel control (CCC) and incomplete channel control (ICC), respectively. Green open squares (red open circles): experimental data for ten highest (lowest) transmission channels. The simulation data represent an average over 50 disorder realizations. The simulation parameters are slab thickness $L = 10$ μm, width $W = 508$ μm, $l_t = 1$ μm, $n_0 = 1.4$, background refractive index $n_1 = 1.0$ (in front of the slab), and $n_2 = 1.5$ (at the back).

such as a sample tilt or an incident wave front tilt. Our model can be extended to other perturbations, such as frequency detuning of the incident light, and provides an understanding of the enhanced bandwidth (spectral memory effect) for high-transmission channels, which was observed previously [21]. Therefore, our work reveals the general characteristic of high-transmission channels: their transmitted fields are robust while their reflected fields are sensitive against perturbations. Thanks to their larger angular memory-effect range, the high-transmission channels provide a wider scan range than Gaussian beams or random wave fronts, which will be useful for improving the quality of memory-effect-based speckle imaging through diffusive or otherwise complex media. Finally, the spatial memory effect was recently discovered in anisotropic scattering systems of length much larger than the scattering mean free path but comparable to or smaller than the transport mean free path [23,24,30]. It will be interesting to investigate the spatial memory effect for the transmission eigenchannels of such systems.

We thank Allard Mosk (Utrecht University) for his comments after critically reading the manuscript. This work is supported partly by the Office of Naval Research (ONR) under Grant No. MURI N00014-13-0649 and by the U.S.-Israel Binational Science Foundation (BSF) under Grant No. 2015509. We acknowledge support from the European Commission under project NHQWAVE (Grant No. MSCA-RISE 691209), as well as the computational resources by the Yale High Performance Computing Cluster (Yale HPC).

*hui.cao@yale.edu

[1] J. Jang, J. Lim, H. Yu, H. Choi, J. Ha, J.-H. Park, W.-Y. Oh, W. Jang, S. Lee, and Y. Park, Opt. Express **21**, 2890 (2013).
[2] S. Kang, S. Jeong, W. Choi, H. Ko, T. D. Yang, J. H. oo, J.-S. Lee, Y.-S. Lim, Q.-H. Park, and W. Choi, Nat. Photonics **9**, 253 (2015).
[3] A. Badon, D. Li, G. Lerosey, A. C. Boccara, M. Fink, and A. Aubry, Sci. Adv. **2**, e1600370 (2016).
[4] Y. Zhao, W. J. Eldridge, J. R. Maher, S. Kim, M. Crose, M. Ibrahim, H. Levinson, and A. Wax, Opt. Lett. **42**, 2302 (2017).
[5] A. Lyons, F. Tonolini, A. Boccolini, A. Repetti, R. Henderson, Y. Wiaux, and D. Faccio, Nat. Photonics **13**, 575 (2019).
[6] A. P. Mosk, A. Lagendijk, G. Lerosey, and M. Fink, Nat. Photonics **6**, 283 (2012).
[7] R. Horstmeyer, H. Ruan, and C. Yang, Nat. Photonics **9**, 563 (2015).
[8] I. M. Vellekoop, Opt. Express **23**, 12189 (2015).
[9] M. Kim, W. Choi, Y. Choi, C. Yoon, and W. Choi, Opt. Express **23**, 12648 (2015).
[10] H. Yu, J. Park, K. Lee, J. Yoon, K. Kim, S. Lee, and Y. Park, Curr. Appl. Phys. **15**, 632 (2015).
[11] S. Rotter and S. Gigan, Rev. Mod. Phys. **89**, 015005 (2017).
[12] J. Bertolotti, E. G. van Putten, C. Blum, A. Lagendijk, W. L. Vos, and A. P. Mosk, Nature (London) **491**, 232 (2012).
[13] K. T. Takasaki and J. W. Fleischer, Opt. Express **22**, 31426 (2014).
[14] O. Katz, P. Heidmann, M. Fink, and S. Gigan, Nat. Photonics **8**, 784 (2014).
[15] H. Yılmaz, E. G. van Putten, J. Bertolotti, A. Lagendijk, W. L. Vos, and A. P. Mosk, Optica **2**, 424 (2015).
[16] X. Li, A. Stevens, J. A. Greenberg, and M. E. Gehm, Sci. Rep. **8**, 13402 (2018).
[17] B. Shapiro, Phys. Rev. Lett. **57**, 2168 (1986).
[18] A. Z. Genack, Phys. Rev. Lett. **58**, 2043 (1987).
[19] J. F. de Boer, M. P. van Albada, and A. Lagendijk, Phys. Rev. B **45**, 658 (1992).
[20] R. Berkovits and S. Feng, Phys. Rep. **238**, 135 (1994).
[21] J. Bosch, S. A. Goorden, and A. P. Mosk, Opt. Express **24**, 26472 (2016).
[22] S. Schott, J. Bertolotti, J.-F. Léger, L. Bourdieu, and S. Gigan, Opt. Express **23**, 13505 (2015).
[23] G. Osnabrugge, R. Horstmeyer, I. N. Papadopoulos, B. Judkewitz, and I. M. Vellekoop, Optica **4**, 886 (2017).
[24] M. Kadobianskyi, I. N. Papadopoulos, T. Chaigne, R. Horstmeyer, and B. Judkewitz, Optica **5**, 389 (2018).
[25] I. Freund, M. Rosenbluh, and S. Feng, Phys. Rev. Lett. **61**, 2328 (1988).
[26] S. Feng, C. Kane, P. A. Lee, and A. D. Stone, Phys. Rev. Lett. **61**, 834 (1988).
[27] R. Berkovits, M. Kaveh, and S. Feng, Phys. Rev. B **40**, 737 (1989).
[28] I. Freund and R. Berkovits, Phys. Rev. B **41**, 496 (1990).
[29] J. H. Li and A. Z. Genack, Phys. Rev. E **49**, 4530 (1994).
[30] B. Judkewitz, R. Horstmeyer, I. M. Vellekoop, I. N. Papadopoulos, and C. Yang, Nat. Phys. **11**, 684 (2015).
[31] I. M. Vellekoop and A. P. Mosk, Opt. Lett. **32**, 2309 (2007).
[32] I. M. Vellekoop and A. P. Mosk, Phys. Rev. Lett. **101**, 120601 (2008).
[33] M. Kim, Y. Choi, C. Yoon, W. Choi, J. Kim, Q.-H. Park, and W. Choi, Nat. Photonics **6**, 581 (2012).
[34] S. M. Popoff, A. Goetschy, S. F. Liew, A. D. Stone, and H. Cao, Phys. Rev. Lett. **112**, 133903 (2014).
[35] R. Sarma, A. G. Yamilov, S. Petrenko, Y. Bromberg, and H. Cao, Phys. Rev. Lett. **117**, 086803 (2016).
[36] W. Choi, A. P. Mosk, Q. Han Park, and W. Choi, Phys. Rev. B **83**, 134207 (2011).
[37] B. Gérardin, J. Laurent, A. Derode, C. Prada, and A. Aubry, Phys. Rev. Lett. **113**, 173901 (2014).
[38] M. Davy, Z. Shi, J. Park, C. Tian, and A. Z. Genack, Nat. Commun. **6**, 6893 (2015).
[39] O. S. Ojambati, H. Yılmaz, A. Lagendijk, A. P. Mosk, and W. L. Vos, New J. Phys. **18**, 043032 (2016).
[40] P. Hong, O. S. Ojambati, A. Lagendijk, A. P. Mosk, and W. L. Vos, Optica **5**, 844 (2018).
[41] H. Yılmaz, C. W. Hsu, A. Yamilov, and H. Cao, Nat. Photonics **13**, 352 (2019).
[42] P. Fang, C. Tian, L. Zhao, Y. P. Bliokh, V. Freilikher, and F. Nori, Phys. Rev. B **99**, 094202 (2019).
[43] H. Yu, J.-H. Park, and Y. Park, Opt. Commun. **352**, 33 (2015).
[44] M. Kim, W. Choi, C. Yoon, G. H. Kim, S.-H. Kim, G.-R. Yi, Q.-H. Park, and W. Choi, Opt. Express **23**, 12740 (2015).

[45] S. Jeong, Y.-R. Lee, W. Choi, S. Kang, J. H. Hong, J.-S. Park, Y.-S. Lim, H.-G. Park, and W. Choi, Nat. Photonics **12**, 277 (2018).

[46] See Supplemental Material at http://link.aps.org/supplemental/10.1103/PhysRevLett.123.203901 for detailed descriptions of the experimental setup, numerical simulations, and the phenomenological model, which includes Refs. [28,34,41,47–50].

[47] C. W. Hsu, S. F. Liew, A. Goetschy, H. Cao, and A. D. Stone, Nat. Phys. **13**, 497 (2017).

[48] I. M. Vellekoop, E. G. van Putten, A. Lagendijk, and A. P. Mosk, Opt. Express **16**, 67 (2008).

[49] A. MacKinnon, Z. Phys. B **59**, 385 (1985).

[50] H. U. Baranger, D. P. DiVincenzo, R. A. Jalabert, and A. D. Stone, Phys. Rev. B **44**, 10637 (1991).

[51] S. M. Popoff, G. Lerosey, R. Carminati, M. Fink, A. C. Boccara, and S. Gigan, Phys. Rev. Lett. **104**, 100601 (2010).

[52] A. Goetschy and A. D. Stone, Phys. Rev. Lett. **111**, 063901 (2013).

Angular memory effect of transmission eigenchannels: supplementary material

Hasan Yılmaz,[1] Chia Wei Hsu,[1,2] Arthur Goetschy,[3] Stefan Bittner,[1] Stefan Rotter,[4] Alexey Yamilov,[5] and Hui Cao[1,*]

[1] *Department of Applied Physics, Yale University, New Haven, Connecticut 06520, USA*
[2] *Ming Hsieh Department of Electrical and Computer Engineering, University of Southern California, Los Angeles, California 90089, USA*
[3] *ESPCI Paris, PSL University, CNRS, Institut Langevin, 1 rue Jussieu, F-75005 Paris, France*
[4] *Institute for Theoretical Physics, Vienna University of Technology (TU Wien), 1040, Vienna, Austria*
[5] *Department of Physics, Missouri University of Science & Technology, Rolla, Missouri 65409, USA*

(Dated: October 8, 2019)

This document provides supplementary information to 'Angular memory effect of transmission eigenchannels'. Here, we elaborate on the experimental setup and measurement procedure, provide details of the numerical simulations and the phenomenological model.

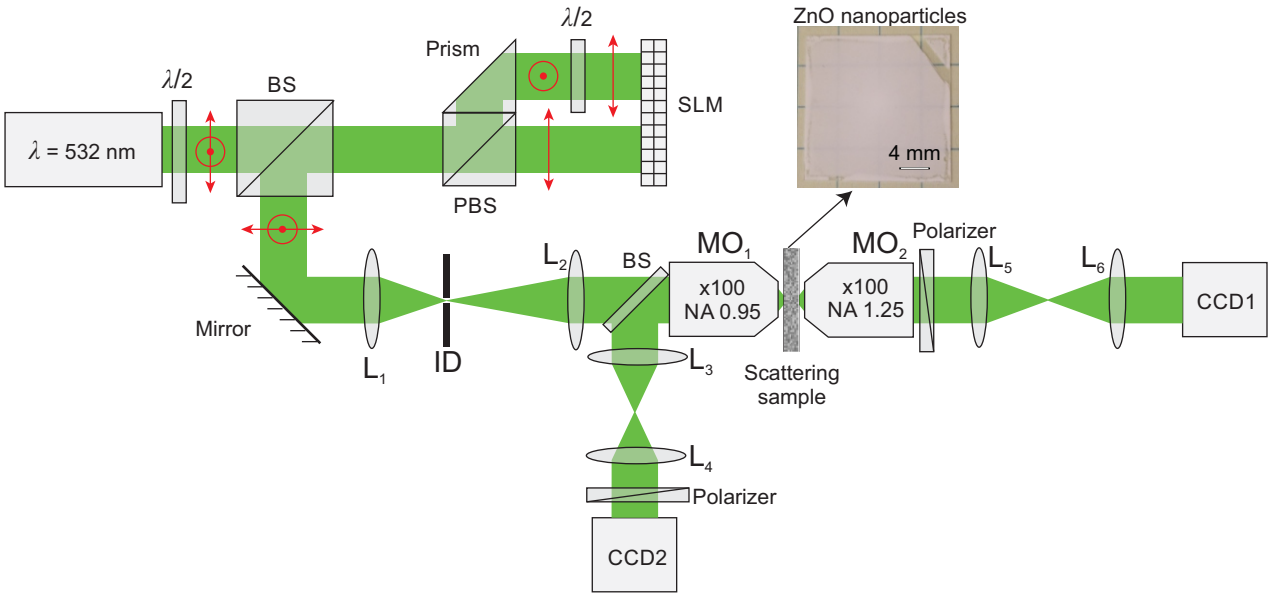

FIG. S1. A detailed sketch of the experimental setup. A reflective phase-only SLM modulates separately the phase-fronts of two orthogonal linear polarization components of a monochromatic laser beam ($\lambda = 532$ nm). The field transmission matrix of the scattering sample is measured in k space with the SLM and the camera CCD1. Inset: an optical image of the scattering sample: a 10 µm-thick film of ZnO nanoparticles on a glass substrate. The camera CCD2 captures the spatial intensity profile of reflected light in k space. $\lambda/2$: half-wave plate. BS: beam splitter. PBS: polarizing beam splitter. $MO_{1,2}$: microscope objectives. L_{1-6}: lenses. ID: iris diaphragm.

Experiment

The sample is made of densely-packed zinc oxide (ZnO) nanoparticles (average diameter $\simeq 200$ nm), deposited on a cover slip of thickness 170 µm. The average transmittance is approximately 0.2. The effective refractive index of the ZnO nanoparticle layer is about 1.4 [1], which closely matches the refractive index of the glass substrate.

* hui.cao@yale.edu

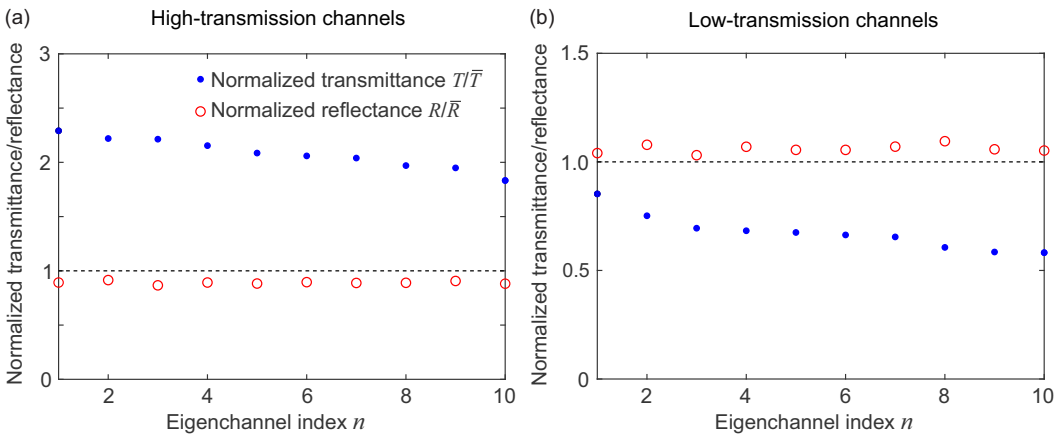

FIG. S2. Experimentally measured transmittance and reflectance of transmission eigenchannels, normalized to the values of random incident wavefronts. (a) The ten highest transmission eigenchannels all have normalized reflectance $R/\overline{R} < 1$. (b) The ten lowest transmission eigenchannels all have normalized reflectance $R/\overline{R} > 1$. The black dashed lines represent $T/\overline{T} = R/\overline{R} = 1$.

A detailed sketch of the experimental setup is presented in Fig. S1. A linearly-polarized monochromatic laser beam (Coherent, Compass 215M-50 SL) with wavelength $\lambda = 532$ nm is expanded and collimated. Its polarization direction is rotated from vertical to 45° by a half-wave ($\lambda/2$) plate, and split into vertical and horizontal polarizations by a polarizing beam splitter (PBS). The horizontal-polarized component of the beam illuminates one part of the SLM (Hamamatsu, X10468-01). Since the SLM only modulates horizontal polarization, the vertically-polarized component of the beam is converted into horizontal polarization by another $\lambda/2$ plate before impinging onto the second part of the SLM; the modulated reflected beam is converted back to vertical polarization after passing through the same $\lambda/2$ plate again. The two polarizations are recombined at the PBS, and the SLM plane is imaged onto the pupil of a microscope objective MO_1 (Nikon CF Plan 100× with a numerical aperture $NA_{in} = 0.95$) by a pair of lenses L_1 and L_2 (with focal lengths $f_1 = 100$ mm and $f_2 = 250$ mm). The reflected light from the ZnO sample is collected by the same objective MO_1, and the far-field intensity distribution on its pupil is imaged onto a camera CCD2 (Allied Vision, Mako G-032B) by a pair of lenses L_{3-4} with focal lengths of $f_3 = f_4 = 200$ mm. A linear polarizer is placed before the camera to select only one polarization of the reflected light.

In transmission, the Fourier transform of the transmitted field on the back (output) surface of the sample is imaged onto another camera CCD1 (Allied Vision, Manta G-031B) by an oil-immersion microscope objective MO_2 (Edmund Optics DIN Achromatic 100×, $NA_{out} = 1.25$) and a pair of lens L_5 ($f_5 = 200$ mm) and L_6 ($f_6 = 150$ mm). The field of view of MO_2 on the back surface of the sample has a diameter of 180 μm. A linear polarizer is placed right after MO_2 to filter out one polarization component of the transmitted light.

The field transmission matrix from the SLM to the CCD1 is measured in Hadamard basis, with a common-path interferometry method [2–4]. 4830 SLM macropixels (2415 per polarization) are imaged onto the entrance pupil of MO_1, covering the entire pupil. Among them, we use 2048 macropixels (1024 per polarization) for the signal field and 2782 macropixels for the reference field in the transmission matrix measurement. Each macropixel consists of 9×9 SLM pixels. A uniform (but fixed) phase pattern is displayed on the reference pixels. To measure the transmitted intensity of the signal field in each Hadamard basis vector, a high-spatial-frequency phase grating is written to the reference region of the SLM so that the reference field is diffracted away from the iris ID.

After measuring the field transmission matrix, we calculate the eigenvectors which represent the input wavefronts for individual transmission eigenchannels using the relation $t^\dagger t V_n = \tau_n V_n$, where V_n is the n-th eigenvector, and τ_n is the corresponding eigenvalue that gives the transmittance of the n-th eigenchannel. After finding the eigenvectors, we block the reference field by imposing a high-spatial-frequency phase grating on the reference region of the SLM. Then we display the phase patterns of the phase-only modulated eigenvectors with the 10 highest and lowest transmittance on the 2048 macropixels of the SLM, and record the transmitted and reflected intensity patterns with CCD1 and CCD2. The transmittance T and reflectance R for these channels are obtained by integrating the patterns, and normalized by the average values shown in Fig. S2. These data confirm that the high (or low) transmission channels have reduced (or enhanced) reflection. Next we gradually shift the phase pattern of each channel on the SLM to tilt its incident wavefront, and record the transmitted and reflected intensity patterns in far field. Each step of the tilt is about 0.2°, and the total range is 3.5°, which is significantly larger than the angular correlation width of the random wavefronts. We repeat this measurement for 20 random incident wavefronts to find the angular memory-effect range.

In principle, adding a linear phase ramp to the incident field on the sample surface by translating the SLM phase pattern does not modify the intensity pattern on the sample surface. However, due to optical aberrations in the setup, the translation in k space slightly modifies the illumination pattern on the sample surface. Such modification depends on the incident beam width on the sample surface, therefore it is different for high-transmission channels which have smaller beam width than low-transmission channels [4]. The modification of the incident intensity pattern would accelerate the decorrelation of transmitted pattern and reduce the angular correlation width. In order to have a fair comparison of the memory-effect range between random wavefronts and transmission eigenchannels, we use the phase-conjugate of the SLM phase patterns of the high/low-transmission eigenchannels as random wavefronts. The transmission eigenchannels and their phase-conjugates have equal incident beam width on the sample surface. However, the phase-conjugate inputs have a transmittance close to the average value, $T/\overline{T} = 1$, as expected from the random wavefronts. We normalize the tilt angle θ in the plot of high/low-transmission channels' intensity correlation functions by the width of their phase-conjugate incident wavefronts' intensity correlation functions, denoted as $\theta/\theta_0^{(\mathrm{r})}$ in Fig. 1(c) of the main text.

Numerical simulations

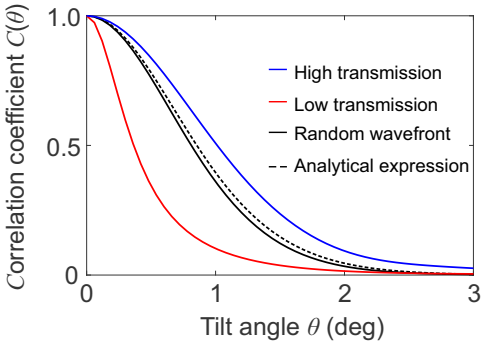

FIG. S3. Numerically calculated intensity correlation function $C(\theta)$ of transmission eigenchannels, in comparison to the random wavefronts and the analytical expression are presented. While $C(\theta)$ of random incident wavefronts (black solid line) agrees well to the analytical expression (black dashed line), an eigenchannel of $\tau_n = 0.999$ (blue solid curve) exhibits a slower decay of $C(\theta)$, while an eigenchannel of $\tau_n = 0.01$ (solid red curve) a faster decay. Each numerical curve represents an average over 10 disorder realizations. Simulation parameters are identical to those in Fig. 2 of the main text.

In our numerical simulations, we calculate wave propagation through two-dimensional (2D) diffusive slabs, $W \gg L \gg l_\mathrm{t}$. The sample is discretized on a 2D square grid, and the grid size is $(\lambda/2\pi) \times (\lambda/2\pi)$. The dielectric constant at each grid point is $\epsilon(\mathbf{r}) = n_0^2 + \delta\epsilon(\mathbf{r})$, where n_0 is the average refractive index of the sample, $\delta\epsilon(\mathbf{r})$ a random number between $[-\Sigma, \Sigma]$ with uniform probability. The sample is sandwiched between two homogeneous media with refractive indices of n_1 and n_2. Periodic boundary conditions are applied to the transverse boundaries. To obtain the field transmission matrix t at wavelength λ, we solve the scalar wave equation $\left[\nabla^2 + k_0^2\epsilon(\mathbf{r})\right]\psi(\mathbf{r}) = 0$ with the recursive Green's function method [5, 6].

After finding incident wavefronts from the eigenvectors of $t^\dagger t$, we calculate the output fields of each eigenchannel by tilting its incident wavefront. The transmitted field is then tilted back by the same angle θ, and its Pearson correlation with the original transmitted field is computed. From the field correlation $C_n^{(\mathrm{E})}(\theta)$, the intensity correlation $C_n(\theta) = |C_n^{(\mathrm{E})}(\theta)|^2$ is obtained. Fig. S3 shows the numerically calculated intensity correlation function $C_n(\theta)$ of random incident wavefronts and of high/low-transmission eigenchannels, as well as the analytical expression given in reference [7] with no freely adjustable parameters. While the analytical correlation function $C(\theta)$ agrees well with the $C(\theta)$ for random incident wavefronts, we observe distinct differences for the high/low-transmission eigenchannels.

We further investigate the scaling of the angular memory-effect range with the sample thickness. We numerically calculate the angular width $\theta_0^{(\mathrm{h})}$ of the intensity correlation function for the average high-transmission channels with $\tau_n > \overline{\tau}$ in diffusive slabs with different thickness L and transport mean free path l_t. As shown in Fig. S4, $\theta_0^{(\mathrm{h})}$ is inversely proportional to the effective sample thickness, $L_\mathrm{eff} = L + 2z_\mathrm{e}$, where $z_\mathrm{e} = 0.818l_t$ is the extrapolation length for the index-matched interfaces. Hence, $\theta_0^{(\mathrm{h})}$ becomes independent of l_t for $L \gg l_\mathrm{t}$.

The slab parameters (refractive indices, transport mean free path, slab thickness) and the parameters that define incomplete channel control used in the numerical simulations for Fig. 3 of the main text, are chosen to be close to those

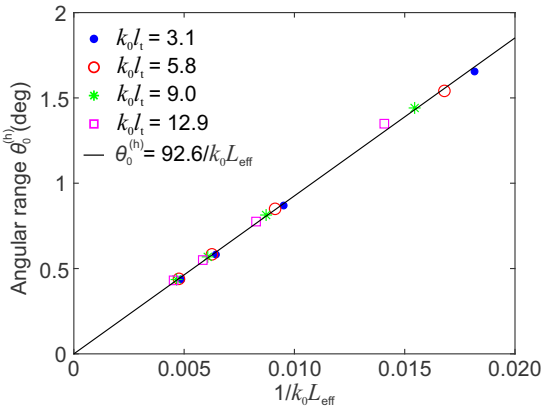

FIG. S4. Scaling of angular correlation width with sample thickness. Numerically calculated angular width $\theta_0^{(\mathrm{h})}$ of the intensity correlation function averaged over high-transmission channels with $\tau_n > \overline{\tau}$, versus the effective sample thickness, $L_{\mathrm{eff}} = L + 2z_{\mathrm{e}}$, where $z_{\mathrm{e}} = 0.818 l_t$. The slabs have different L and l_{t}, but the same width $k_0 W = 3000$ and average refractive index $n_0 = 1.5$. Each data point represents an average over 10 disorder realizations.

of our experiment with the ZnO nanoparticle layer. The slab ($n_0 = 1.4$) is sandwiched between air ($n_1 = 1.0$) and glass ($n_2 = 1.5$). In case of complete control, the number of input modes (from the air) is $M_1 = 1999 \approx 2n_1 W/\lambda$, and the number of output modes (to the glass) $M_2 = 3239$. To model the effect of incomplete control on the angular-memory effect of transmission eigenchannels, we apply the following procedures on the complete transmission matrices. Due to the limited numerical aperture (NA) in the illumination and the detection, and single polarization detection, the number of experimentally accessible columns (input modes) and rows (output modes) of the transmission matrix is reduced. To numerically model such reduction of the transmission-matrix size, we take only 1024 columns and 1155 rows of the k-space transmission matrices in our simulations. Moreover, to model the binning of SLM pixels into macropixels, we group the columns in k-space. The number of columns in one group, $m_1 = 32$, is chosen such that the corresponding illumination width on the front surface of the slab is similar to that in the experiment. Such truncation and grouping the columns effectively reduce the number of degrees of freedom to $M_1^{(\mathrm{eff})} = 32$ at the input. We did not group the output modes, since the detection field of view is larger than the beam width at the output in the experiment. To model the incomplete detection for the reflection memory effect in the simulations (Fig. 3(b) in the main text), we apply exactly the same truncation and grouping to the columns of the reflection matrices, but take only 1024 out of 1999 number of rows of the reflection matrices.

Phenomenological model

Here we present the details of our phenomonological model for the angular memory effect of transmission eigenchannels and the complete derivation of the intensity correlation function C_n in Eq. (1) of the main text.

The n-th transmission eigenchannel has the input state $|V_n\rangle$, which is associated to the transmission eigenvalue τ_n by the relation:

$$t^\dagger t \, |V_n\rangle = \tau_n \, |V_n\rangle \, . \tag{S1}$$

Here t is the field transmission matrix whose singular value decomposition reads

$$\begin{aligned} t &= U \tau^{1/2} V^\dagger \\ &= \sum_k |U_k\rangle \, \tau_k^{1/2} \, \langle V_k| \, , \end{aligned} \tag{S2}$$

so that $t \, |V_n\rangle = \sqrt{\tau_n} \, |U_n\rangle$ is the output associated to V_n.

When the diffusive slab is tilted by an angle θ, the output state becomes $t_\theta \, |V_n\rangle$. We define the intensity correlation

function between the two output states as

$$C_n(\theta) \equiv \frac{|\langle V_n| t^\dagger t_\theta |V_n\rangle|^2}{\langle V_n| t^\dagger t |V_n\rangle \langle V_n| t_\theta^\dagger t_\theta |V_n\rangle} = \frac{|\langle U_n| t_\theta |V_n\rangle|^2}{\langle V_n| t_\theta^\dagger t_\theta |V_n\rangle}. \tag{S3}$$

The sample tilt is equivalent to the operation that consists in tilting the illumination wavefront by an angle θ, applying the transmission matrix t, and tilting back the scattered wavefront by $-\theta$. Thus t_θ can be expressed as

$$t_\theta = R_\theta^\dagger \, t \, R_\theta, \tag{S4}$$

where R_θ is the tilting matrix and can be written in real space as

$$R_\theta = \mathrm{e}^{\mathrm{i}k\theta\hat{\rho}}, \tag{S5}$$

where $\hat{\rho}$ represents the transverse coordinate on the front surface of the sample. For $\theta \ll 1$, $R_\theta \simeq \mathbb{1} + \mathrm{i}k\theta\hat{\rho}$, where $\mathbb{1}$ is the identity matrix. This suggests to model the tilting matrix R_θ as

$$R_\theta = \mathbb{1} + X, \tag{S6}$$

where X is an $N \times N$ complex Gaussian random matrix, whose elements satisfy the following relations in the channel basis:

$$\overline{X_{ij}} = 0, \tag{S7}$$

$$\overline{X_{ij} X_{i'j'}^*} = (\sigma^2/N)\delta_{ii'}\delta_{jj'}. \tag{S8}$$

Here the random matrix elements are averaged over ensembles. This model is phenomenological because we replace the deterministic matrix R_θ by a random matrix. According to the decompositions (S2) and (S4), and the model (S6), the numerator of the correlation function C_n becomes

$$\begin{aligned} |\langle U_n| t_\theta |V_n\rangle|^2 &= |\langle U_n| (1+X^\dagger) t (1+X) |V_n\rangle|^2 \\ &= |\sqrt{\tau_n} + \sqrt{\tau_n}\langle U_n| X^\dagger |U_n\rangle + \sqrt{\tau_n}\langle V_n| X |V_n\rangle + \langle U_n| X^\dagger t X |V_n\rangle|^2 \\ &= \tau_n |1 + \langle U_n| X^\dagger |U_n\rangle + \langle V_n| X |V_n\rangle|^2 + |\langle U_n| X^\dagger t X |V_n\rangle|^2 \\ &\quad + 2\mathrm{Re}\left[\left(1 + \langle U_n| X^\dagger |U_n\rangle + \langle V_n| X |V_n\rangle\right)\langle V_n| X^\dagger t^\dagger X |U_n\rangle\right]. \end{aligned} \tag{S9}$$

We expand each term in the channel basis and proceed to the average over the matrix X, using Gaussian contraction rules and Eqs. (S7) and (S8). The average of the numerator becomes

$$\overline{|\langle U_n| t_\theta |V_n\rangle|^2} = (1 + 2\sigma^2/N)\tau_n + \sigma^4\bar{\tau}/N, \tag{S10}$$

where $\bar{\tau} = \mathrm{Tr}(t^\dagger t)/N$. Similarly, the expression for the denominator of the correlation function C_n is written as

$$\langle V_n| t_\theta^\dagger t_\theta |V_n\rangle = \langle V_n| (\mathbb{1} + X^\dagger) t^\dagger (\mathbb{1} + X)(\mathbb{1} + X^\dagger) t (\mathbb{1} + X) |V_n\rangle. \tag{S11}$$

We average this expression, keeping only the terms that involve the same number of matrices X and $X^\dagger$, and using $\mathrm{Tr}(t) \simeq 0$ we obtain

$$\langle V_n| \overline{t_\theta^\dagger t_\theta} |V_n\rangle \simeq (1+\sigma^2)(\tau_n + \sigma^2\bar{\tau}). \tag{S12}$$

Finally, by combining Eqs. (S10) and (S12), we get the following expression for the mean of the correlation function:

$$\overline{C_n} = \frac{(1 + 2\sigma^2/N)\tau_n + \sigma^4\bar{\tau}/N}{(1+\sigma^2)(\tau_n + \sigma^2\bar{\tau})}. \tag{S13}$$

For $\sigma^2 \ll N$, $\overline{C_n}$ is well approximated by

$$\overline{C_n} \simeq \frac{1}{1+\sigma^2}\frac{\tau_n + \sigma^4\bar{\tau}/N}{\tau_n + \sigma^2\bar{\tau}}. \tag{S14}$$

We found that this result provides a good fit of our simulations for arbitrary tilt angle θ. For $\theta \ll 1$ rad, the decomposition (S6) applies with $X \simeq \mathrm{i}k_0\theta\hat{\rho}$. Hence, we expect in this limit the scaling $\sigma^2 = \overline{\mathrm{Tr}X^\dagger X}/N \propto \theta^2$. Our numerical analysis reveals that the scaling prefactor is $\sigma^2/\theta^2 \propto (k_0 L_{\mathrm{eff}})^2$. This is consistent with the numerical results showing that the angular correlation width of the open channels scales as $\theta_0^{(\mathrm{h})} \propto 1/(k_0 L_{\mathrm{eff}})$ (see Fig. S4).

The phenomenological model can be applied to reflection matrices r, and the mean of the intensity correlation function in reflection $\overline{C_n^{(\mathrm{R})}}$ can be derived in the same way:

$$\overline{C_n^{(\mathrm{R})}} \simeq \frac{1}{1+\sigma^2}\frac{(1-\tau_n)+\sigma^4(1-\bar{\tau})/N}{(1-\tau_n)+\sigma^2(1-\bar{\tau})}. \tag{S15}$$

Hence, the reflected pattern stays more correlated for low-transmission channels (with high reflectance); when the reflection eigenvalue $\rho_n = 1-\tau_n \gg \sigma^2$, $\overline{C_n^{(\mathrm{R})}}$ approaches unity. In contrast, the reflected pattern decorrelates faster for high-transmission channels (low reflectance); for $\rho_n = 1-\tau_n \to 0$, the correlation function $\overline{C_n^{(\mathrm{R})}}$ is on the order of $1/N$, which is the expected value between two uncorrelated speckle patterns with N speckle grains. Although we do not probe the reflection eigenchannels explicitly in our experiment, we measure the reflectance of transmission eigenchannels and find that high (low) transmission channels have low (high) reflectance (Fig. S2). According to the phenomenological model, the reflection eigenchannels with high reflectance (low transmittance) have stronger correlation and larger memory effect than the eigenchannels with low reflectance (high transmittance).

[1] I. M. Vellekoop, E. G. van Putten, A. Lagendijk, and A. P. Mosk, "Demixing light paths inside disordered metamaterials," Opt. Express **16**, 67–80 (2008).

[2] S. M. Popoff, G. Lerosey, R. Carminati, M. Fink, A. C. Boccara, and S. Gigan, "Measuring the transmission matrix in optics: an approach to the study and control of light propagation in disordered media," Phys. Rev. Lett. **104**, 100601 (2010).

[3] C. W. Hsu, S. F. Liew, A. Goetschy, H. Cao, and A. D. Stone, "Correlation-enhanced control of wave focusing in disordered media," Nat. Phys. **13**, 497–502 (2017).

[4] H. Yılmaz, C. W. Hsu, A. Yamilov, and H. Cao, "Transverse localization of transmission eigenchannels," Nat. Photonics **13**, 352—358 (2019).

[5] A. MacKinnon, "The calculation of transport properties and density of states of disordered solids," Z. Phys. B **59**, 385—390 (1985).

[6] H. U. Baranger, D. P. DiVincenzo, R. A. Jalabert, and A. D. Stone, "Classical and quantum ballistic-transport anomalies in microjunctions," Phys. Rev. B **44**, 637–675 (1991).

[7] I. Freund and R. Berkovits, "Surface reflections and optical transport through random media: coherent backscattering, optical memory effect, frequency, and dynamical correlations," Phys. Rev. B **41**, 496–503 (1990).